In situ fringe projector development for thermal coating deposition

Nicholas D. Trail
Michael W. Kudenov
Eustace L. Dereniak

In situ fringe projector development for thermal coating deposition

Nicholas D. Trail,[a,*] Michael W. Kudenov,[b] and Eustace L. Dereniak[a]
[a]University of Arizona, College of Optical Sciences, 1630 East University Boulevard, Tucson, Arizona 85721, United States
[b]North Carolina State University, Department of Electrical and Computer Engineering, 890 Oval Drive, Raleigh, North Carolina 27606, United States

Abstract. Thermal barrier coatings (TBCs) and plasma spray coatings, in general, require fine control over the deposited thickness to achieve a reliable coating performance. Currently, the plasma spray industry quantifies thickness by sampling the part before and after TBC deposition. Approximate thickness is inferred from previous runs; however, process variability can cause errors in these approximations that result in wasted time and resources that can ultimately lead to nonreliant coatings. To this end, we present an *in situ* optical fringe projector technology that enables coating thickness measurements across a two-dimensional surface. The sensor is capable of achieving micron scale resolution in the harsh environment of a thermal spray booth. Furthermore, unlike the existing approaches, this technique is extendable to parts with complex geometries. The underlying background of the fringe projection method, including a differential measurement technique, is presented. Current results on production equipment and cylindrical parts are also discussed, showing good correlation and agreement with physical measurements captured in an industrial setting. © *The Authors. Published by SPIE under a Creative Commons Attribution 3.0 Unported License. Distribution or reproduction of this work in whole or in part requires full attribution of the original publication, including its DOI.* [DOI: 10.1117/1.OE.53.7.074105]

Keywords: fringe projection; thermal spray; interferometry; profilometry.

Paper 140882 received May 30, 2014; revised manuscript received Jun. 12, 2014; accepted for publication Jun. 12, 2014; published online Jul. 14, 2014.

1 Introduction

Thermal barrier coatings (TBCs) are a key technology enabler in many industrial applications, such as spanning aerospace, automotive, and energy. These coatings are typically deposited on metal components to provide protection from harsh operational environments; specifically, they prevent part failure by selectively increasing resistance to corrosion, elevated temperatures, and abrasion.[1,2] Due to the important role that these coatings play for increasing a part's reliability, maintaining the coating's quality during deposition is critical. The most fundamental parameter to control during the coating's application is the deposited material's thickness (50–250 μm thick) and uniformity. Yet, this has historically been difficult to measure on actual parts.[3] Rather, approximate thickness is inferred from previous runs; e.g., the number of required torch passes equals the desired thickness divided by the empirically measured thickness per torch pass. Validation involves measuring the thickness using eddy current sensors, calipers, or micrometers after the coating has already been deposited. This inferred procedure leaves the process open to changes in the coating's deposition parameters, leading to reduced yield and reliability.

A successful application of thermally sprayed coatings relies on many interrelated variables. Small deviations in these variables (e.g., torch power, arc strike, powder size distributions, booth ventilation, gas flow rates, etc.) can create a substantially different coating in terms of both geometry and reliability.[4–6] To compensate for these errors, process variables are currently maintained by implementing process controls on the impact plume's properties, including particle velocity, diameter, temperature, and dispersion.[7–9] Yet, even with this feedback, coating failures and yield issues still persist, especially on critical components that operate near the temperature, thermal cycling, and high-velocity impact limits of the material and coating. Ultimately, since many of these procedures do not test the deposited coating, increased time and resources are required to assess pass or fail criteria. Thus, an *in situ* thickness measurement of the coating would help to understand the real-time variations of the process, enabling more consistent results. Furthermore, an active mechanism to understand the coating thickness and uniformity would help both designers and fabricators to optimize the numerous variables based on the direct real-time feedback.

With the aim of increasing reliability and coating yield, several noncontact thickness gauge approaches have been demonstrated, such as photothermal (PT) or laser-ultrasonic (LU) techniques.[10] However, utilization of these technologies is limited by the inherent complexity and costs, and usually requires *a priori* knowledge of the coating properties or geometry, which adds additional complexity and uncertainty. Furthermore, the spray process imparts a significant temperature gradient to the part's substrate. This causes the part to expand; a situation PT and LU techniques are inadequate to compensate against. This type of error means that the measured coating thickness could have a smaller magnitude than the net substrate's thermal expansion. Finally, optical techniques such as line projection have been successfully attempted; however, their applicability is limited to simpler part geometries[11]

In this paper, a viable approach to *in situ* coating thickness measurement is described. Leveraging the sensitivity of optical interferometric methods while ruggedizing it for use in the harsh environment of thermal spray production, we demonstrate a fringe projection sensor that enables real-time per-pass thickness measurements. This new approach

*Address all correspondence to: Nicholas D. Trail, E-mail: ntrail@optics.arizona.edu

allows for the direct measurement of the coating layer's thickness, independent of material properties, and thermal expansion. To this end, Sec. 2 describes the basic theory and operational concept for the fringe projector and Sec. 3 discusses the laboratory and production spray booth devices. This is, then, followed by Sec. 4, which provides our results and discussions. Finally, a summary of our results is provided in Sec. 5.

2 Background: Fringe Projection

In fringe projection, the target under test is illuminated with an off-axis sinusoidal intensity pattern. After including a triangulation factor, this projected pattern modulates the three-dimensional spatial information of the target onto its phase. Comparison of the measured phase to that of a reference measurement taken of a flat planar target enables one to relate the measured phase to the sample's physical depth. An illustration of the fringe projector's geometry is provided in Fig. 1.

The geometry of Fig. 1 shows that the projected sinusoid's illumination is incident onto the reference plane at an angle θ_0 with an observed fringe period p_0.[12] The detected reference plane intensity can be represented at point C by

$$I_C = a(x, y) + b(x, y) \cos(2\pi OC/p_0), \tag{1}$$

where $a(x, y)$ is the background light level, $b(x, y)$ is the modulation or contrast of the sinusoid, and O is the origin, which is defined as the intersection of the optical axis with the reference plane. Therefore, Eq. (1) establishes a reference phase $\phi_R = 2\pi OC/p_0$. When the reference is removed and the sample is measured at point D, the detected sample plane intensity can be expressed as

$$I_D = r(x, y)[a(x, y) + b(x, y) \cos(2\pi OE/p_0)], \tag{2}$$

where $r(x, y)$ is the sample's reflectivity. The phase difference, $\Delta\phi_{CD}$ between points C (the reference measurement) and D (the sample measurement), can be related to the distance EC by

Fig. 1 Optical geometry for measuring the 3-D surface profile using fringe projection. Adapted from Ref. 12.

$$EC = (p_0/2\pi)\Delta\phi_{CD}. \tag{3}$$

Assuming θ_n is small,[12] it means that the physical distance between the reference and sample surfaces can be calculated as

$$FD = EC \tan \theta_0. \tag{4}$$

Thus, measuring the phase difference $\Delta\phi_{CD}$ can be accomplished at each spatial location within the scene. Such a phase extraction can be achieved within a single snapshot using Fourier transform techniques.[13–18] Expressing Eqs. (1) and (2) in terms of the general spatial coordinates (x, y) yields

$$I_R = a(x, y) + b(x, y) \cos(2\pi x/p_0) \tag{5}$$

and

$$I_S(x, y) = r(x, y)\{a(x, y) \\ + b(x, y) \cos[2\pi x/p_0 + \Delta\phi_{CD}(x, y)]\}, \tag{6}$$

where the spatial frequency is assumed to vary only along the x dimension. Taking the two-dimensional (2-D) Fourier transformation of Eqs. (5) and (6) yields

$$\mathfrak{F}[I_R(x, y)] = A + B * \delta(\xi - 1/p_0) + B * \delta(\xi + 1/p_0) \tag{7}$$

and

$$\mathfrak{F}[I_S(x, y)] = R * [A + B * \mathfrak{F}[e^{-i\Delta\phi_{CD}(x,y)}] * \delta(\xi - 1/p_0) \\ + B * \mathfrak{F}[e^{i\Delta\phi_{CD}(x,y)}] * \delta(\xi + 1/p_0)], \tag{8}$$

where (ξ, η) are the Fourier transform variables of (x, y), while A, B, and R are the Fourier transforms of a, b, and r, respectively, δ is the Dirac delta function, and $*$ stands for the convolution operation. Note that A, B, and R are implicitly dependent upon (ξ, η). Fourier filtering one of the sideband's delta functions in both the reference and sample data yields

$$C_{REF}(\xi, \eta) = B * \delta(\xi + 1/p_0), \tag{9}$$

and

$$C_{SAMP}(\xi, \eta) = R * B * \mathfrak{F}[e^{i\Delta\phi_{CD}(x,y)}] * \delta(\xi + 1/p_0). \tag{10}$$

Inverse Fourier transformation of C_{REF} and C_{SAMP} produces two exponential functions within the spatial domain

$$c_{REF}(x, y) = B(x, y)e^{i2\pi x/p_0}, \tag{11}$$

and

$$c_{SAMP}(x, y) = R(x, y)B(x, y)e^{i2\pi x/p_0}e^{i\Delta\phi_{CD}(x,y)}. \tag{12}$$

Finally, division of Eq. (12) by Eq. (11) demodulates the sample data as

$$\Phi(x, y) = R(x, y)e^{i\Delta\phi_{CD}(x,y)}. \tag{13}$$

Taking the argument of Eq. (13) extracts the phase information $\Delta\phi_{CD}(x, y)$. The surface's depth can then be calculated using Eqs. (3) and (4).
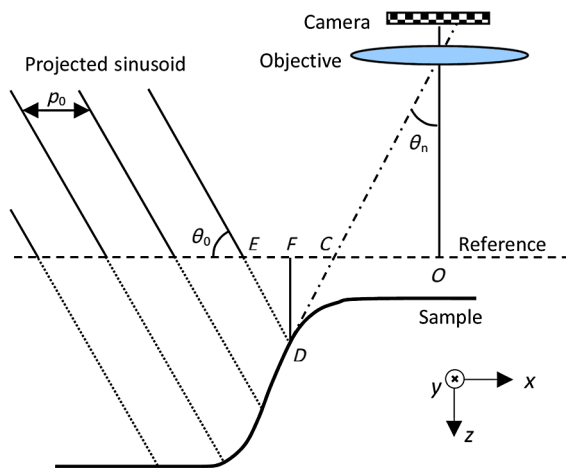
2.1 Differential Measurement Approach

Accuracy in the aforementioned measurement methodology relies on critically measuring the phase difference between the sample and reference planes. Typically, the designs of such systems are configured to avoid any modulo 2π phase unwrapping errors.[19] This leads to the assumption that the target geometry is smoothly varying within the region of a single fringe. For thermal spray this is often the case, as most surface coatings have continuous derivatives (smoothly varying geometry as imparted by the plasma process). However, other sources of phase ambiguity and error can arise due to part motion. Herein, we refer to such motion errors as "jitter," or "jitter error." For instance, a nominal part undergoing thermal spray may be mounted on a spindle chuck, rotating in excess of 300 rotations per minute (RPM), with a run-out greater than 12.5 mm. This translates into a variable imager-to-object distance versus time. Unaccounted for, this error is substantially larger than the micrometer level changes in coating thickness that we are attempting to measure.

As part of our system development, we selected a fringe period ρ_0 to maintain the peak-to-peak phase error caused by jitter to within $\pm\pi/2$. Additionally the jitter error is compensated by incorporating a single object-based reference frame in combination with a differential technique between two separate regions on the target's surface. While differential measurements to compensate jitter have been implemented by others in past research using line projection,[11] its application to fringe projection within the context of thermal spray, to the best of our knowledge, has not been studied.

By incorporating a differential approach, we can reduce the measurement's sensitivity to target jitter. However, there are also differential effects that occur due to the geometry of the target or part. Part geometry can be accounted for with a measuring pass prior to the coating process's start, thus acquiring a part-dependent reference image. The differential operation is described by expanding $\Delta\phi_{CD}(x, y)$ in Eq. (13) to include both the part's geometry and the coating's thickness for two unique spatial locations in the scene. This geometry is depicted in Fig. 2 for a cylindrical target of radius R_S. In this case, a reference frame is taken of the uncoated but sandblasted (e.g., diffusely reflecting) part. At a later time, the coating is deposited on the surface at the previously measured location. However, due to jitter, it is separated by a distance d_j away from the original reference plane. To quantify d_j and to isolate it from the coating thickness d_c, two points are compared: one with (D_1) and the other without (D_2) the coating.

Assuming that θ_{n1} and θ_{n2} are close to 90° enables us to use Eq. (13) as before to calculate the phase $\Delta\phi_{CD}(x, y)$ at both locations D_1 and D_2, yielding $\Delta\phi_{CD_1}$ and $\Delta\phi_{CD_2}$, respectively. These phase terms can be represented as a combination of the coating's thickness d_c and the jitter separation d_j as

$$\Phi_1 = R_1 e^{i\Delta\phi_{CD_1}} = R_1 e^{i2\pi d_j/\lambda_{EQ}}, \tag{14}$$

and

$$\Phi_2 = R_2 e^{i\Delta\phi_{CD_2}} = R_2 [e^{i2\pi d_j/\lambda_{EQ}} + e^{-i2\pi d_c/\lambda_{EQ}}], \tag{15}$$

where λ_{EQ} is the equivalent wavelength, expressed as

$$\lambda_{EQ} = \rho_0 \tan\theta_0. \tag{16}$$

Taking the argument of Eqs. (14) and (15) yields

$$\phi_1 = 2\pi d_j/\lambda_{EQ}, \tag{17}$$

and

$$\phi_2 = 2\pi(d_j - d_c)/\lambda_{EQ}. \tag{18}$$

The difference of the arguments results in the differential phase term, with both the geometry and coating effects present. Subtracting ϕ_1 from ϕ_2 isolates the coating's thickness from the measurement such that

$$\Delta\phi_{1-2} = 2\pi d_c/\lambda_{EQ}. \tag{19}$$

An example of this differential technique is illustrated in Fig. 3, which depicts an image of a stainless steel witness coupon as viewed under fringe illumination. This coupon has a layer of yttria-stabilized zirconia (YSZ) on the right half (denoted by box labeled "A") and sandblasted metal on the left half (box "B"). Following any fringe (black or white line), there is a noticeable phase shift in the transition from the bare metal to the YSZ deposited layer at this magnification. This relates to a change in thickness between the two regions due to the coating. In the differential measurement approach, two regions are identified on separate sides of the image that are aligned with the torch's motion. By treating one as the reference, a snapshot differential phase measurement can be produced.

Assuming the plasma torch deposits the coating material over the surface moving from the right to the left in Fig. 3(a), then the increase in thickness would be detected by box (a) before box (b). This change can be directly related to an increase in the coating's thickness. Applied more generally, as depicted in Fig. 3(b), this differential (single frame) measurement approach can occur over many points in the image at once. For instance, Fig. 3(b) demonstrates that if the image was broken up into 5×5 zones, then the phase difference across the image could be measured and calibrated to the thickness across a 2-D space. This approach assumes that
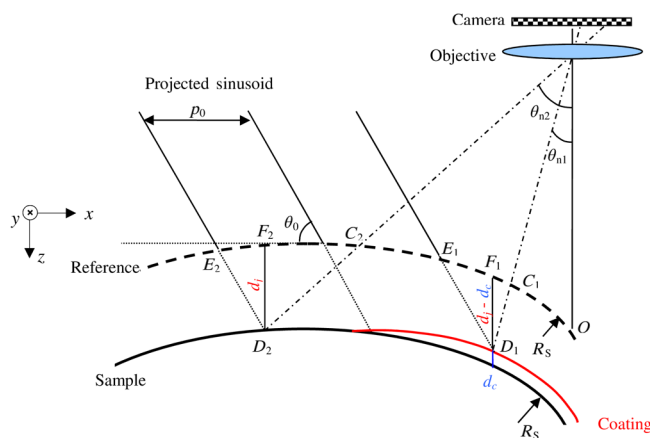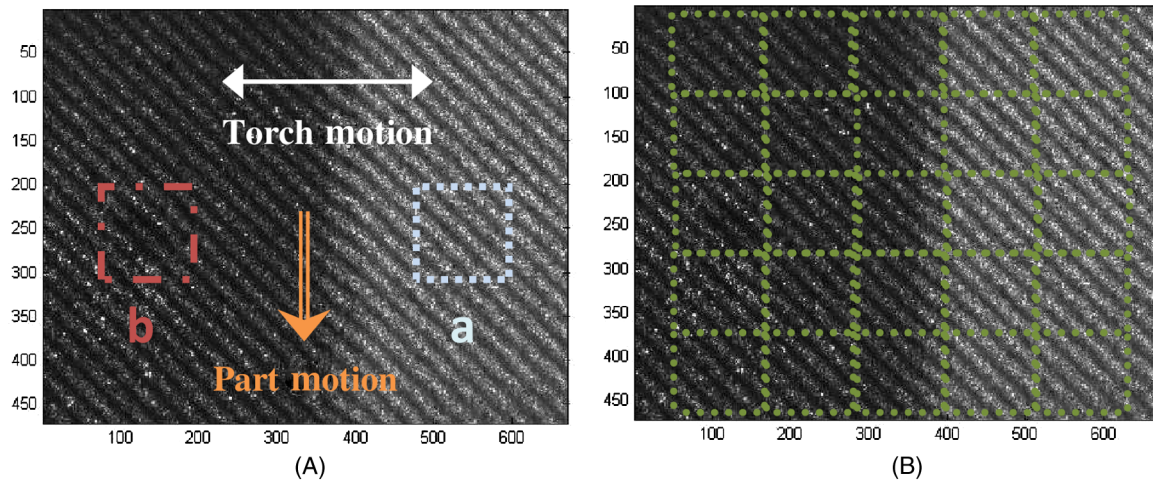

Fig. 2 Exaggerated geometry for performing the differential phase measurement. The reference measurement is now a frame taken from the data of the part without coating. Vibration and jitter create a phase shift away from the reference plane upon a subsequent measurement.

Fig. 3 (A) Example image of surface under fringe illumination, coated (a) and bare substrate (b), and (B) demonstrated image division to extract 2-D phase map.

the plasma torch's spot size is small; less than half of the camera's field of view (FOV), in addition to a frame rate that is high enough to capture the torch at several positions across the FOV. This allows a significant increase in sampling points and measuring area for any given snapshot and for each individual coating pass. Thus, by measuring these individual passes and summing the total phase change during the transitions, a measurement of the overall coating thickness can be determined across the part's surface.

3 Laboratory Prototype

A laboratory prototype was developed as a proof of concept for the fringe projector's differential measurement technique. In this approach, the fringes are generated and projected onto the target of interest, forming a non-normal angle relative to the plasma stream's direction and the imaging camera path. This approach is captured in Fig. 4, showing relative geometry and orientation.
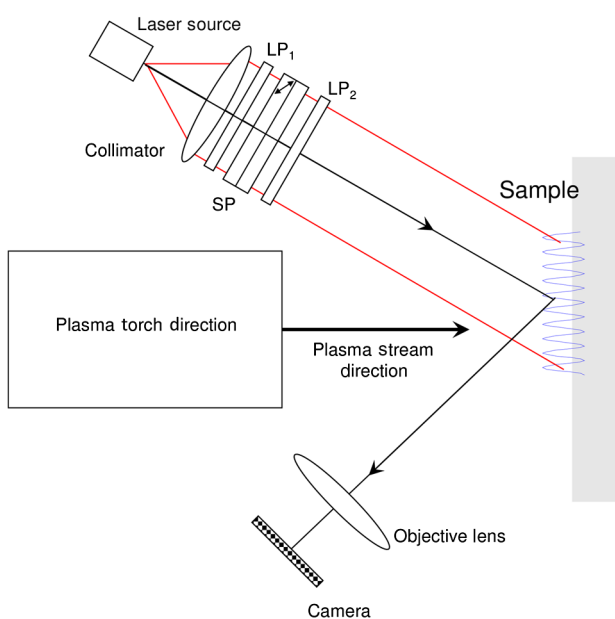

Fig. 4 Block diagram of fringe projector operation with thermal spray operation.

The fringe projector assembly is shown schematically in Fig. 5(a), while an image of the completed (but unsealed) prototype is depicted in Fig. 5(b). A 650-nm laser diode (average output power around one (1) Watt, continuous wave) was chosen. This wavelength allows for a nearly maximized detector response while simultaneously avoiding peak spectral emission lines from the plasma, as is shown from plasma gas mixture measurements per Fig. 6.

A lens was used to nearly collimate the laser diode and present a slightly diverging optical wavefront through the linear polarizers (LP_1 and LP_2) and Savart plate (SP). Note that in Fig. 5(a), this diverging beam is exaggerated to illustrate the operational concept. The first linear polarizer (LP_1) was orientated parallel to the laser's linear polarization state to maximize the laser's output power. The SP was then set at 45° (extraordinary and ordinary index vectors) relative to LP_1 in order to split equal power into both of the SP's eigenstates. For an SP, the net shear distance is

$$S_{SP} = \sqrt{2}\Delta = \sqrt{2}\frac{n_e^2 - n_o^2}{n_e^2 + n_o^2}t, \tag{20}$$

which is related to the thickness of an SP (thickness $2t$) and the ordinary and extraordinary refractive indices (n_o and n_e, respectively).[20] The final polarizer, LP_2, sets the fringe coherence by combining the two polarization states, enabling interference fringes to be localized at the sample. Note that the small divergence of the beam results in a projected fringe frequency that depends on the distance between the projector and object. While error is expected from varying object distances, this error is within approximately 0.1% given a 1.0% error in projector-to-object distance induced by jitter. While this approach is prone to some small error, it was chosen because it provides an effective means to vary the fringe frequency by adjusting the beam's divergence. This allowed us to select a fringe frequency that was large enough to maintain the jitter within modulo 2π phase.

The fringe illuminator assembly was then mounted in a sealed aluminum tube to prevent degradation of the optics from particulates and powder debris in the coating chamber. The imaging side of this setup was an industrial CMOS detector, capable of integrating down to a minimum of three (3) microseconds, to minimize rotation-induced motion
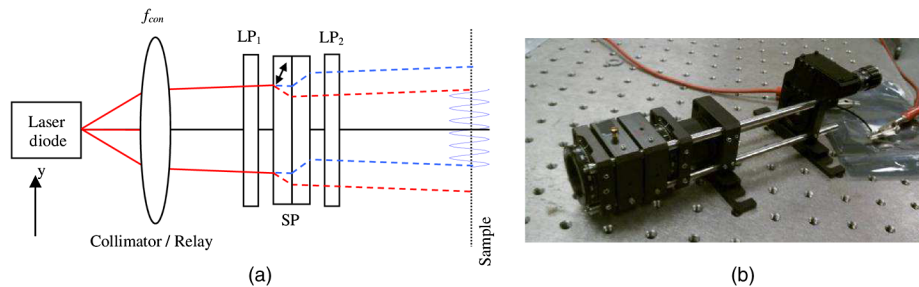
Fig. 5 Optical path for the fringe projector assembly (a), and the as-completed prototype layout (b).
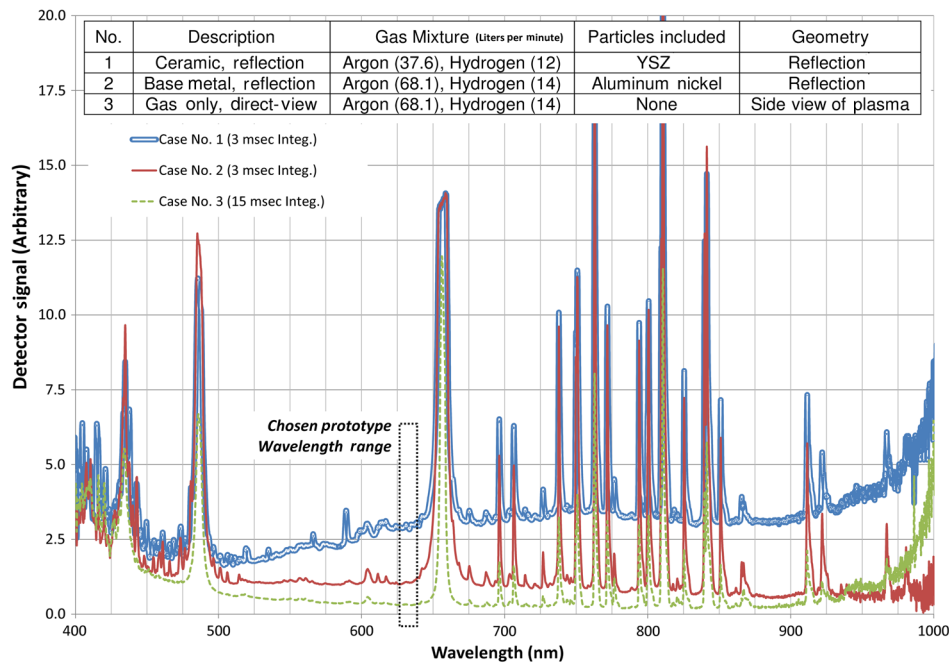

Fig. 6 Measured thermal spray plasma gas relative output spectrum.

blur. A notional view of the setup is depicted in Fig. 7, where the full sensor geometry is shown relative to a rotation target in Fig. 7(b). It is also noted, that in this approach, a remote trigger is provided in order to sync measurements to a repeatable position. Here, we have accomplished triggering through an optical pickup and reflective tape per Fig. 7(b) at one location. In this orientation, the robot is moved vertically, which is parallel to the long dimension and the cylinder's rotation axis.

4 In Situ Testing Results

In order to validate the approach and fringe projection method, the sensor was tested in conventional thermal spray booth configurations. As shown in Fig. 8(a), the sensor was mounted in a production booth to measure deposited metal coatings (nickel substrate). During this trial, a 100-mm diameter cylindrical stainless steel substrate, approximately 300 mm long, was mounted in a rotation chuck that was operated at 300 RPM. The fringe projection sensor was mounted to a tripod that was positioned perpendicular to the plasma stream [Fig. 8(b)], while the camera was triggered by an optical pickup and reflective tape to measure a repeatable area. Utilizing this approach, the robot moved up and

down the rotating part, depositing a thin coating layer on each pass. The sensor took an image on each rotation and created a database of measurements over the course of approximately 6 min. Indexing each measurement according to time and displaying the full time sequential database, Fig. 9 shows the unaltered measurement phase (green and blue lines), and the extracted actual deposition measurements (red line) utilizing the differential approach. In fact, without the differential technique, the induced jitter from this setup masks any single-pass measurements that are clearly depicted in the peaks and nulls of the jitter compensated dataset, although the general increase in phase from the full coating is visible in the trend of both the uncorrected measurements.

4.1 Processed Results and Analysis

Processing and calibrating the jitter-compensated results of Fig. 9 yield the calibrated data depicted in Fig. 10. Starting at time $t = 0$ s, the plasma torch is first moved over the target to provide uniform heating (no powder), which registers a spike in the dataset. The torch then returns to the "home" position as it awaits a stable feed of powder stock (denoted as no activity from approximately 40–130 s). After this point,
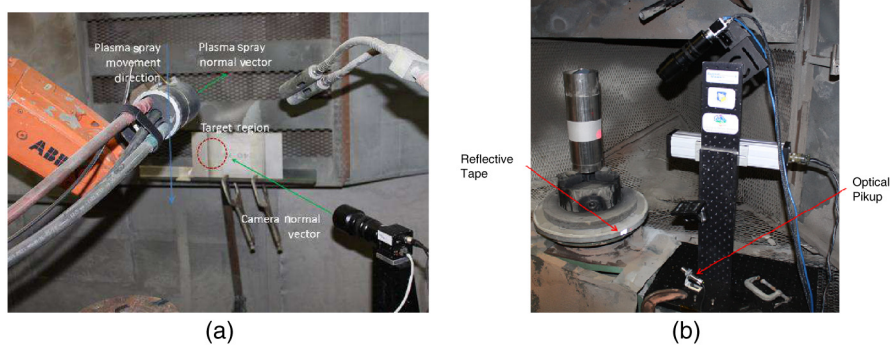
Fig. 7 Orientation of camera and fringe projector (not shown) relative to plasma spray (a), and full fringe projector sensor geometry as shown with a rotation sample (b).
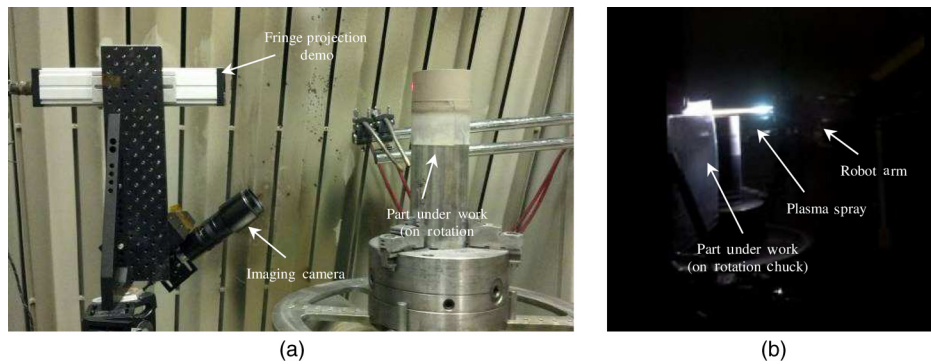

Fig. 8 Side-view of the fringe projection system geometry (a) with plasma torch out of page view, and snapshot of in situ deposition measurement (b) of a cylindrical sample.
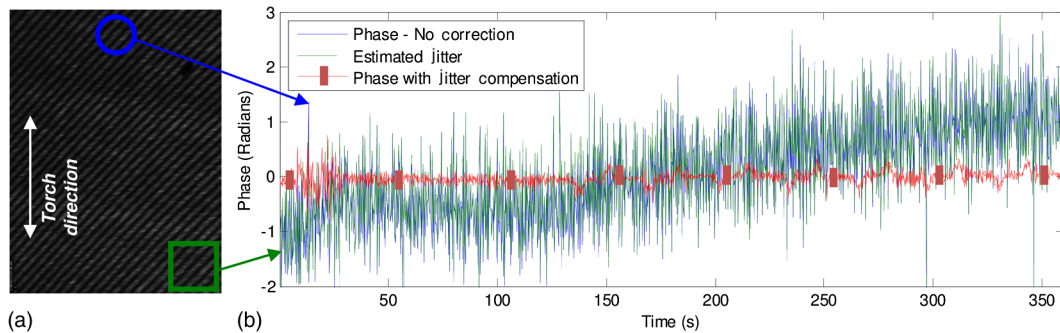

Fig. 9 Extracted single image (a), and (b) phase versus time during the deposition process.
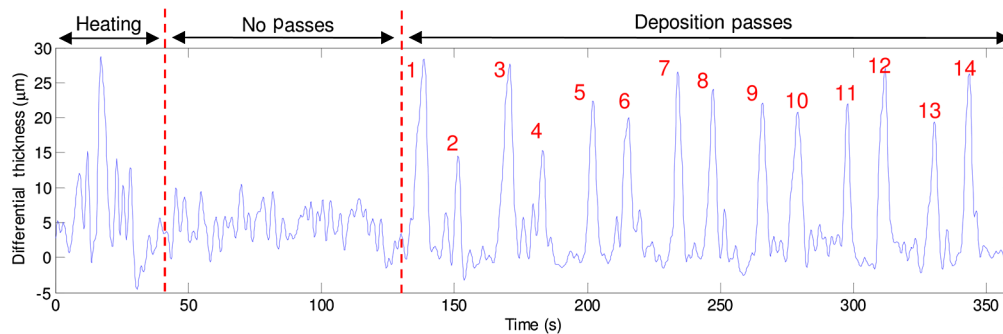

Fig. 10 (Differential) measured single-pass metal base coating as-deposited on cylindrical steel target.

the plasma operation proceeds with the coating passes (14 individual passes), which are captured for the next approximately 230 s. These are denoted by an individual pass number in Fig. 10. Each single-pass measurement is then accumulated to yield the total deposited coating thickness. This operation calculated a coating thickness of 316 ± 20 μm, where the traditional measurement, taken with a digital caliper, estimated 330 ± 25 μm; this is less than 5% deviation and well within a significant value for both. The instrumental accuracy was calculated by taking the standard deviation during the "no pass" image set from the time block of 40 to 130 s, while the micrometer measurement was averaged over four measurements across both the inner and outer diameters, to mitigate heating and localized point effects.

5 Conclusion

The fringe projection approach was demonstrated as a viable *in situ* coating thickness measurement technique, accurate to the micron level, by accumulating thickness changes on individual plasma coating deposition passes. Results were shown on metallic plasma coatings in an *in situ* measurement environment. Measurements from the system agreed with conventional data taken with a caliper. Overall, this novel measurement capability will allow improved control for a key thermal barrier coating deposition, and demonstrates a practical manner to implement in an industrial setting.

In the future, this technique could allow the operator to measure numerous points at a significantly faster rate than currently allowed through the use of automation and 2-D data acquisition over the target surface. This would provide real-time feedback on the coating results, decrease operator dependence for physical measurements and downtime, increase yield, and enable more optimal control of coating tolerances.

References

1. National Materials Advisory Board/National Research Council. *Coatings for High-Temperature Structural Materials*, National Academy Press, Washington, DC (1996).
2. J. T. DeMasi-Marcin and D. K. Gupta, "Protective coatings in the gas turbine engine," *Surf. Coat. Technol.* **68–69**, 1–9 (1994).
3. C. Sung, J. W. Ryul Hutchinson, and A. G. Evans, "Delamination of multilayer thermal barrier coatings," *Mech. Mater.* **31**(7), 431–447 (1999).
4. P. Fauchais, "Formation of plasma sprayed coatings," *J. Therm. Spray Technol.* **4**(1), 3–6 (1995).
5. W. Beele, G. Marijnissen, and A. van Lieshout, "The evolution of thermal barrier coatings: status and upcoming solutions for today's key issues," *Surf. Coat. Technol.* **120–121**, 61–67 (1999).
6. G. Dwivedi et al., "Assessing process and coating reliability through monitoring of process and design relevant coating properties," *J. Therm. Spray Technol.* **19**(4), 695–712 (2010).
7. P. Fauchais, "Understanding plasma spraying," *J. Phys. D: Appl. Phys.* **37**(9), R86–R108 (2004).
8. P. Marc, P. Gougeon, and C. Moreau, "Structure of plasma-sprayed zirconia coatings tailored by controlling the temperature and vecolity of the sprayed particles," *J. Therm. Spray Technol.* **10**(1), 67–75 (2001).
9. M. Vardelle et al., "Controlling particle injection in plasma spraying," *J. Therm. Spray Technol.* **10**(2), 267–284 (2001).
10. L. Fabbri and M. Oksanen, "Characterization of plasma-sprayed coatings using nondestructive evaluation techniques: round-robin test results," *J. Therm. Spray Technol.* **8**(2), 263–272 (1999).
11. A. Nadeau et al., "A new approach to online thickness measurement of thermal spray coatings," *J. Therm. Spray Technol.* **15**(4), 744–749 (2006).
12. V. Srinivasan, H. C. Liu, and M. Malioua, "Automated phase-measuring profilometry of 3-D diffuse objects," *Appl. Opt.* **23**(18), 3105–3108 (1984).
13. M. W. Kudenov et al., "White light Sagnac interferometer for snapshot multipsectral imaging," *Appl. Opt.* **49**(21), 4067–4076 (2010).
14. M. Kudenov et al., "Prismatic imaging polarimeter calibration for the infrared spectral region," *Opt. Express* **16**(18), 13720–13737 (2008).
15. M. W. Kudenov et al., "White light Sagnac interferometer for snapshot linear polarimetric imaging," *Opt. Express* **17**(25), 22520–22534 (2009).
16. H. Luo et al., "Compact and miniature snapshot imaging polarimeter," *Appl. Opt.* **47**(24), 4413–4417 (2008).
17. F. Chen, G. Brown, and M. Song, "Overview of three-dimensional shape measurement using optical methods," *Opt. Eng.* **39**(1), 10–22 (2000).
18. X. Su and W. Chen, "Fourier transform profilometry: a review," *Opt. Laser Eng.* **35**(5), 263–284 (2001).
19. D. C. Ghiglia and M. D. Pritt, *Two-Dimensional Phase Unwrapping: Theory, Algorithms, and Software*, John Wiley & Sons, New York (1998).
20. M. Daniel, *Optical Shop Testing*, John Wiley & Sons, New York (2007).

Nicholas D. Trail received his BS and MS degrees in optical science and engineering in 2007 and 2010, respectively, and anticipates completing his PhD degree in optical sciences in 2015 from the University of Arizona, Tucson, Arizona. He also works for a major defense company as a senior optical engineer, where he designs and develops visible to far-infrared, passive and laser-based electro-optical systems.

Michael W. Kudenov received his BS degree in electrical and computer engineering from University of Alaska Fairbanks, Fairbanks, Alaska, in 2005 and his PhD degree in optical sciences from the University of Arizona, Tucson, Arizona, in 2009. He is an assistant professor of ECE at North Carolina State University in Raleigh, North Carolina. His lab researches compact high-speed hyperspectral, polarimetric, and interferometric sensors and sensing systems within multidisciplinary applications spanning remote sensing, defense, process monitoring, and biological imaging. He is a member of SPIE.

Eustace L. Dereniak is a professor of optical sciences and electrical and computer engineering at the University of Arizona, Tucson, Arizona. He is a co-author of several textbooks, including *Optical Radiation Detectors, Infrared Detectors and Systems*, published by Wiley-Interscience, and *Geometrical and Trigonometrical Optics*, published by Cambridge Press. He has written chapters in *Imaging in Medicine*, edited by S. Nudelman and D. Patton, related to research and development using thermograph instrumentation for the early detection of breast cancer. His publications also include over 100 authored or co-authored refereed articles. He is a fellow of SPIE and OSA, and a president of SPIE in 2012.